Acta Astronautica 212 (2023) 329–338

Contents lists available at ScienceDirect

Acta Astronautica

journal homepage: www.elsevier.com/locate/actaastro

Research paper

Computational characterization of the temperature field in coaxial nitrogen injection under supercritical conditions

Leandro B. Magalhães [a,b,*], André R.R. Silva [a], Jorge M.M. Barata [a]

[a] AEROG-LAETA, University of Beira Interior, 6201-001, Covilhã, Portugal
[b] ISEC, ISEC Lisboa, Alameda das Linhas de Torres 179, 1750-142 Lisboa, Portugal

ARTICLE INFO

Keywords:
Transcritical mixing
Supercritical mixing
Liquid rocket engines

ABSTRACT

The modeling of fluids in the supercritical regime is addressed at conditions characteristic of liquid-propelled rocket engines, whose increasing performance demands paved the way for supercritical conditions. In the present document, nitrogen is used as a surrogate for the commonly encountered oxygen-hydrogen mixture so that turbulence mixing can be looked into without influences from combustion and chemically reacting effects. The temperature field validation on nitrogen coaxial injection at supercritical conditions, with high-velocity ratios (outer-to-inner), where the main (inner) stream is recessed relative to the outer stream, is of paramount importance in the flame stabilization operation of liquid rocket motors. The temperature field is analyzed taking into account varying momentum and velocity ratios, whose increased leads to a reduction of potential core lengths, increasing jet spreading. The results also depict a fundamental influence of thermal effects, dominating over the transport of momentum. The experimental data and large eddy simulation solvers from the literature agree with the estimate of injection velocities at several conditions and comparable to the space shuttle main engine pre-burner.

1. Introduction

Working fluids' critical temperature and pressure are often exceeded in the pursuit of higher efficiencies in propulsive systems [1–3]. In conditions labeled supercritical, fluids exhibit distinct behaviors than subcritical ones. For instance, the critical point marks the end of the gas–liquid discontinuity and is characterized by the critical divergence of thermal conductivity and specific heat [4], while other properties such as latent heat and surface tension go to zero. Consequently, these fluids exhibit characteristics intermediate between those of liquids and gases, whereas mass diffusivity replaces vaporization as the governing parameter over jet atomization [5].

The seeming homogeneity of the supercritical regime has been disproved since the coexistence line between liquid and gas phases extends into the supercritical regime, denoting a fundamental change from liquid-like conditions into gas-like ones, being the division called Widom or pseudo-critical line [6]. The transition process can be traced back to the temperature where the isobaric specific heat is maximum, a process called pseudo-boiling occurring in a narrow temperature range and relevant for pressure up to three times that of the critical point [6]. At supercritical conditions, the energy a fluid receives has different impacts on jet evolution depending on liquid- or gas-like conditions [7]. At liquid-like conditions, the jet mechanical breakup description is used [7]. Here the steepest thermophysical property gradients are encountered, and the energy received by the jet primarily contributes to its expansion instead of its heating [8]. On the other hand, at supercritical gas-like conditions, thermal effects play a preponderant role, the term 'thermal breakup' coined [7] and used to explain discrepancies between experiments and simulations in a canonical nitrogen injection experiment [9].

Canonical quantitative experimental data [9–11] remain the go-to studies for validating numerical efforts attempting to model the non-linear behavior of fluid flows under supercritical conditions. Several numerical studies [1,12–20] have dealt with the subject of supercritical fluid flow modeling, resorting to computational techniques ranging from Reynolds-averaged Navier–Stokes (RANS) and Large Eddy Simulation (LES) to fundamental studies in the context of Direct Numerical Simulation. While representing essential steps toward a deeper understanding of the flow physics governing supercritical flows, there is still a lack of consensus about which mechanism governs jet disintegration.

Moreover, the focus has been mostly [1,7,12–16,18–20] on single injection, mainly looking into the density field evolution. Studies on coaxial injection at supercritical conditions have been few and far between. For instance, a hybrid RANS/LES [21] was employed to assess how the non-linearity thermophysical parameters are coupled

* Corresponding author at: AEROG-LAETA, University of Beira Interior, 6201-001, Covilhã, Portugal.
E-mail addresses: leandro.magalhaes@iseclisboa.pt (L.B. Magalhães), andre@ubi.pt (A.R.R. Silva), jbarata@ubi.pt (J.M.M. Barata).

https://doi.org/10.1016/j.actaastro.2023.08.004
Received 28 June 2023; Received in revised form 28 July 2023; Accepted 4 August 2023
Available online 9 August 2023

with turbulence mixing and its enhancement at supercritical conditions. Further, LES studies [22] detailed injector geometry and operating conditions that influence the re-circulation in the near field. At the same time, the formation of finger-like structures [23] on the jet breakup and its connection to pseudo-boiling was also looked into. On a more fundamental nature, DNS [24] focusing on acoustic excitation effect showed good agreement at velocity and momentum ratios representative of the space shuttle pre-burner.

The typical operation of liquid rocket engines (LREs) requires the coaxial injection of a mixture of propellants. Due to the development of Kelvin–Helmholtz instabilities, coaxial injection is initially governed by the outer shear layer growth. Then, as the injection process continues to take place, the low-speed jet discharged from the central orifice entrains into the faster coaxial one, forming the inner shear layer through a mass transfer process acting as a separation between inner potential core and shear layer [25,26]. Furthermore, a re-circulation is expected in the near field due to the momentum ratio between the outer and inner jets. At low-pressure coaxial injection conditions, the re-circulation region development is highly affected by the velocity profile shape [27]. In contrast, at supercritical conditions, the temperature profile will play a preponderant role both at gas-like [7] and liquid-like conditions [20].

Given that coaxial injection under supercritical conditions is a subject that has been sparingly explored in the literature, except very few studies [21–24], mainly focusing on a single injection condition, in the present work we propose to look into several injection conditions [11] at varying outer-to-inner jet velocity and momentum ratios to be able to draw a bigger picture regarding the behavior of the fluid flows under consideration.

The remaining manuscript is organized as follows: the mathematical, physical, and numerical methods and models used are discussed in 2, starting with the governing equations, turbulence modeling choices, and the thermophysical parameter non-linear behavior, detailed the Equation of State and the transport properties. Then a summary of their discretization is undertaken. Next, the computational domain is discussed in 3, while a grid sensitivity analysis is described in 4. Finally, numerical results detailing several outer-to-inner jet velocity and momentum ratios are depicted in 5, and the main findings are summarized in 6.

2. Thermophysical and numerical models

2.1. Governing equations

Eqs. (1), (2) and (3), express the conservation principles of mass, momentum, and energy, respectively, where Favre averages detail the variable density nature of the flow under consideration. In the equations, ρ is the density, u_i the velocity in the ith direction, x_j the direction, p the pressure, τ_{ij} the viscous stress tensor, H the total enthalpy and q_j the heat flux. While the flow behavior in a rocket combustor is an inherently oscillatory 3-D process [28–30], a 2-D axisymmetric configuration is followed in the present study as highlighted in Eqs. (1) to (3). The justification comes from the conditions in which quantitative experimental measurements of supercritical fluid flows are carried out [9–11,31]. Typically, a cool-down period allows establishing steady state conditions [11] in the experimental setup, particularly between the chamber and the injector.

$$\frac{\partial \overline{\rho}\tilde{u}_i}{\partial x_i} = 0 \tag{1}$$

$$\frac{\partial}{\partial x_j}\left(\overline{\rho}\tilde{u}_i\tilde{u}_j\right) = -\frac{\partial \overline{p}}{\partial x_i} + \frac{\partial \overline{\tau_{ij}}}{\partial x_j} - \frac{\partial \overline{\rho}\widetilde{u_i'' u_j''}}{\partial x_j} \tag{2}$$

$$\frac{\partial \overline{\rho}\tilde{u}_j \tilde{H}}{\partial x_j} = \frac{\partial \overline{\tau_{ij}u_i}}{\partial x_j} - \frac{\partial \tilde{u}_i \overline{\rho}\widetilde{u_i'' u_j''}}{\partial x_j} - \frac{\partial\left(\overline{q}_j + \overline{\rho}\widetilde{u_j'' h''}\right)}{\partial x_j} \tag{3}$$

The Reynolds stress tensor $-\overline{\rho}\widetilde{u_i'' u_j''}$ is given following equation (4), Following Boussinesq's hypothesis, where κ is the turbulence kinetic energy, δ_{ij} Kronecker's delta and μ_t the eddy viscosity.

$$-\overline{\rho}\widetilde{u_i'' u_j''} = -\frac{2}{3}\rho k\delta_{ij} + \mu_t\left(\frac{\partial \tilde{u}_i}{\partial x_j} + \frac{\partial \tilde{u}_j}{\partial x_i} - \frac{2}{3}\frac{\partial \tilde{u}_k}{\partial x_k}\delta_{ij}\right) \tag{4}$$

The turbulence heat flux $\overline{\rho}\widetilde{u_j'' h''}$ is described in Eq. (5), being Pr_t the turbulent Prandtl number, T the temperature and c_p the isobaric specific heat.

$$\overline{\rho}\widetilde{u_j'' h''} = -\frac{c_p \mu_t}{\mathrm{Pr}_t}\frac{\partial \tilde{T}}{\partial x_j} = -\frac{\mu_t}{\mathrm{Pr}_t}\frac{\partial \tilde{h}}{\partial x_j} \tag{5}$$

Eddy viscosity is evaluated according to Eq. (6), where ϵ is the turbulence kinetic energy dissipation. Turbulence kinetic energy and its dissipation are evaluated from Eqs. (7) and (8), respectively [32]. The remaining terms in the equations are constants defined as $\sigma_\kappa = 1.0$, $\sigma_\epsilon = 1.3$, $C_\mu = 0.09$, $C_{\epsilon 1} = 1.35$, $C_{\epsilon 2} = 1.8$ and $f_1 = 1.0$.

$$\mu_t = C_\mu f_\mu \frac{\rho\kappa^2}{\epsilon} \tag{6}$$

$$\frac{\partial(\rho u_j \kappa)}{\partial x_j} = \tau_{ij}\frac{\partial \tilde{u}_i}{\partial x_j} - p\epsilon + \frac{\partial}{\partial x_j}\left[\left(\mu + \frac{\mu_t}{\sigma_\kappa}\right)\frac{\partial \kappa}{\partial x_j}\right] \tag{7}$$

$$\frac{\partial(\rho u_j \epsilon)}{\partial x_j} = C_{\epsilon 1} f_1 \frac{\epsilon}{\kappa}\tau_{ij}\frac{\partial \tilde{u}_i}{\partial x_j} - C_{\epsilon 2} f_2 \frac{\rho\epsilon^2}{\kappa} + \frac{\partial}{\partial x_j}\left[\left(\mu + \frac{\mu_t}{\sigma_\epsilon}\right)\frac{\partial \epsilon}{\partial x_j}\right] \tag{8}$$

2.2. Equation of state and transport properties

Cubic equations of state, whose general formulation is given according to Eq. (9), are an attractive choice due to the compromise between their simplistic formulation, accuracy, and computational cost. R is the gas constant, v the specific volume, b the inter-molecular repulse potential, a the inter-molecular attractive potential, while δ_1 and δ_2 are parameters that depend on the equation of state used. The present work uses the Peng–Robinson [33] since earlier studies [34] showed its good accuracy at supercritical conditions. It is obtained by taking δ_1 to be $1+\sqrt{2}$ and $\delta_2 = 1-\sqrt{2}$.

$$p = \frac{RT}{v-b} - \frac{a(T)}{\left(v+\delta_1 b\right)\left(v+\delta_2 b\right)} \tag{9}$$

The various coefficients arising from this formulation, namely the attractive potential, correlation function, and molecular volume, are presented in Eqs. (10) to (13), where subscripts c and r represent critical point and reduced conditions, respectively and ω is the acentric factor to account for the non-sphericity of the molecules.

$$a(T) = a(T_c).a\left(T_r, \omega\right) \tag{10}$$

$$a(T_c) = 0.45724\frac{R^2 T_c^2}{p_c} \tag{11}$$

$$a\left(T_r, \omega\right) = \left[1 + \left(0.37464 + 1.54226\omega - 0.26992\omega^2\right)\left(1 - \sqrt{T_r}\right)\right]^2 \tag{12}$$

$$b = b_c = 0.07780\frac{RT_c}{p_c} \tag{13}$$

Thermodynamic properties are evaluated with the departure function formalism, where ideal property values are added corrections to account for real gas and compressibility effects. Examples are given in Eqs. (14) and (15) for the internal energy and enthalpy, respectively. These correspond to exact representations owing to Maxwellian and thermodynamic potential definitions [35].

$$e(p,T) = e_0(T) + \int_{\rho_0}^{\rho}\left[\frac{p}{\rho^2} + \frac{T}{\rho^2}\left(\frac{\partial p}{\partial T}\right)_\rho\right]_T d\rho \tag{14}$$

$$h(p,T) = h_0(T) + \int_{p_0}^{p}\left[\frac{1}{\rho} + \frac{T}{\rho^2}\left(\frac{\partial \rho}{\partial T}\right)_p\right]_T dp \tag{15}$$

The ideal gas enthalpy ($h_0(T)$) component is calculated with the 7 coefficient NASA polynomials [36] of Eq. (16), being the coefficients a_1 to a_6 tabulated constants [36].

$$\frac{h_0(T)}{\mathcal{R}T} = a_1 + a_2\frac{T}{2} + a_3\frac{T^2}{3} + a_4\frac{T^3}{4} + a_5\frac{T^4}{5} + a_6\frac{1}{T} \tag{16}$$

At this point, the integral of the right-hand side of Eqs. (14) and (15) is evaluated, taking into account the equation of state used and converting it to an explicit thermal formulation [35], as detailed in Eqs. (17) and (18), with Z being the compressibility factor. Lastly the partial derivative $\frac{\partial a}{\partial T}$ is evaluated from Eq. (19).

$$\frac{e(p,T) - e_0(T)}{\mathcal{R}T} = \frac{a(T)a\left(T_r,\omega\right) - T\frac{\partial a}{\partial T}}{\mathcal{R}T\sqrt{8b^2}} \ln\left(\frac{2v + 2b - \sqrt{8b^2}}{2v + 2b + \sqrt{8b^2}}\right) \tag{17}$$

$$\frac{h(p,T) - h_0(T)}{\mathcal{R}} = \frac{a(T)a\left(T_r,\omega\right) + T\frac{\partial a}{\partial T}}{\mathcal{R}T\sqrt{8b^2}} \ln\left(\frac{2v + 2b - \sqrt{8b^2}}{2v + 2b + \sqrt{8b^2}}\right) - 1 + Z \tag{18}$$

$$\frac{\partial a}{\partial T} = -\frac{\left(0.37464 + 1.54226\omega - 0.26992\omega^2\right)a(T_c)}{T_c T_r^{1/2}} \tag{19}$$

Transport properties such as dynamic viscosity and thermal conductivity are evaluated similarly with the departure function formalism [37].

$$\mu = \mu^0(T) + \mu^r(\rho_r, T_r) \tag{20}$$

Ideal gas dynamic viscosity is evaluated according to Eq. (21), where $\mathcal{M}$ is the molar mass, σ the Lennard-Jones size parameter and Ω is the collision integral, described in Eq. (22), while the residual dynamic viscosity component is calculated from Eq. (23). The remaining variables in Eqs. (22) to (23) are tabulated constants for nitrogen [37].

$$\mu^0(T) = \frac{0.0266958\sqrt{\mathcal{M}T}}{\sigma^2\Omega(T^*)} \tag{21}$$

$$\Omega(T^*) = \exp\left(\sum_{i=0}^{4} b_i\left[\ln(T^*)\right]^i\right) \tag{22}$$

$$\mu^r(\rho_r, T_r) = \sum_{i=1}^{n} N_i \rho_r^{t_i} T_r^{d_i} \exp\left(-\gamma_i T_r^{l_i}\right) \tag{23}$$

Similarly, thermal conductivity's evaluation follows the same principle as dynamic viscosity with one mild exception. Due to thermal conductivity's critical divergence [4], an additional term is included [38] to improve the accuracy. In this regard, thermal conductivity is evaluated from Eq. (24), taking into account ideal gas component [37] ($\lambda^0(T)$), real gas effects [37] ($\lambda^r(\rho_r, T_r)$) and critical divergence [38] ($\lambda^c(\rho_r, T_r)$). Ideal gas thermal conductivity is evaluated from Eq. (25), dependent on ideal gas viscosity, while the departure function is given by Eq. (25), being the remaining parameters tabulated constants [37]. Eq. (27) details the critical divergence component [38], where $\tilde{\Omega}$ and $\tilde{\Omega}_0$ are dependent on the isobaric and isochoric specific heats, being the remaining parameters tabulated constants [38].

$$\lambda = \lambda^0(T) + \lambda^r(\rho_r, T_r) + \lambda^c(\rho_r, T_r) \tag{24}$$

$$\lambda^0(T) = N_1\left[\frac{\mu^0(T)}{1\ \mu\text{Pa s}}\right] + N_2\rho_r^{t_2} + N_3\rho_r^{t_3} \tag{25}$$

$$\lambda^r(\rho_r, T_r) = \sum_{i=1}^{n} N_i \rho_r^{t_i} T_r^{d_i} \exp\left(-\gamma_i T_r^{l_i}\right) \tag{26}$$

$$\lambda^c = \rho c_p \frac{\kappa_B R_0 T}{6\pi\xi\mu(T,\rho)}\left(\tilde{\Omega} - \tilde{\Omega}_0\right) \tag{27}$$

2.3. Numerical discretization

Diffusive fluxes in the governing equations are discretized using the second-order accurate central scheme, whereas advective fluxes are discretized using the third-order accurate QUICK scheme [39]. It is documented in the literature [40] that a RANS-based strategy is adequate to avoid the formation of non-physical pressure oscillations [40] when the Péclet cell-based number is more than two and a transition over the Widom line occurs. Four nodal points are required, assuming that the normal component of velocity has the same sign for each two opposite walls [39]. It may also be interpreted as a linear interpolation, with a term proportional to the upstream curvature, given that for a parabola, the slope halfway between two points is equal to the chord joining these points. While grid refinement could, in principle, alleviate the problem, its required level would be impracticable for most engineering applications. While dissipation is recognized as the key to controlling oscillatory numerics, high-order schemes are not the only way of introducing it to the computations since sensors of localized artificial viscosity can alternatively be used [41].

A pressure-based method is employed [42], to assure mass conservation using a pressure-based continuity equation. The pressure and velocity fields are then produced concurrently using a staggered grid arrangement owing to the significant coupling of the related phenomena. Finally, significant amounts of under-relaxation aid in achieving a balance between computational burden and accuracy. For steady state simulations, it is recommended to use the highest possible levels of under-relaxation since it accelerates the solution's convergence. Furthermore, it is practical since it can help avoid the divergence of the iterative solution in the presence of strongly non-linear equations. First, however, it is necessary to verify if the converged solution is affected by the values of the under-relaxation factors used. As such, under-relaxation is applied as follows: first, a high level of under-relaxation is applied to the variables that have reached convergence. A lower level of under-relaxation is then applied, and the iterative solver is restarted for about 100–200 iterations. If the lower under-relaxation has no significant influence on the residuals, the solution is independent of the under-relaxation factors used.

3. Computational domain

The coaxial injection of nitrogen into a nitrogen-quiescent environment is explored in this paper, with an emphasis on temperature field validation using quantitative experimental data [11].

The computational domain is shown in Fig. 1, where the main stream measures 50 mm in length and has an inner diameter d_1 of 0.508 mm and an outer diameter d_2 of 1.59 mm. Furthermore, the coaxial stream has an inner diameter of 2.42 mm and an outside diameter of 3.18 mm. The main stream is recessed with respect to the coaxial one by half of d_1, a characteristic widely known in liquid rocket propulsion as a means of flame stabilization [43]. Furthermore, the combustion chamber measures 59.4 mm in length and 76 mm in width, with a depth of 12.7 mm. Following prior studies [20], the injector and chamber walls are represented as isothermal, with the injector faceplate modeled as an adiabatic wall. A constant axial velocity is imposed at the main and coaxial inlets [11], while the radial component is zero. At the adiabatic and isothermal walls the no-slip condition is imposed, while a gauge pressure of 0 MPa is imposed at the domain's outlet. Heat flux at the walls is modeled following equation (28), where q is the heat flux, h_f the heat transfer coefficient and T_w the temperature at the wall. A zero heat flux is imposed in the case of the adiabatic wall and a Dirichlet boundary conditions for the isothermal ones, in accordance to the temperature in the chamber [11].

$$q = h_f\left(T_w - T_\infty\right) \tag{28}$$

A wall function is needed since the $\kappa - \epsilon$ [32] is not valid up to the solid wall. As such a y^+ value of 11.63 is maintaining in

Table 1
Experimental test matrix [11].

Case	p_∞ [MPa]	T_∞ [K]	T_i [K]	T_o [K]	v_i [m s^{-1}]	v_o [m s^{-1}]	VR [-]	M [-]
9	4.97	240	128	188	2.9	4.4	1.5	0.5
10	4.95	237	129	190	3.0	10.9	3.6	2.7
11	4.94	228	133	185	3.9	16.8	4.3	5.1
12	4.94	233	132	191	3.6	22.5	6.3	9.6
SSME	4.94	233	132	191	32	120	3.75	3.44
16	3.54	228	121	136	2.6	4.1	1.5	0.6
17	3.53	202	120	140	2.6	11.0	4.2	3.9
18	3.52	197	119	135	2.5	15.6	6.1	9.4
19	3.54	197	125	134	3.1	18.5	5.9	11.2
20	4.97	218	128	137	2.9	3.6	1.2	0.8
21	4.88	203	127	139	2.9	10.5	3.7	6.3

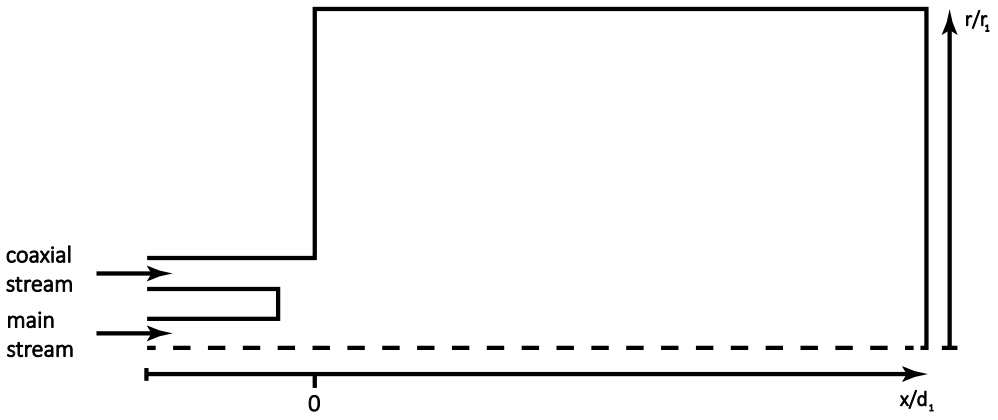

Fig. 1. Representation of the computational domain.

the first cells close to the solid walls, above which the flow is fully turbulent. Moreover, around 20 cells are ensured to be located inside the boundary layer so that it is properly resolved. In terms of initial conditions, the turbulence kinetic energy and its dissipation are set according to Eqs. (29) and (30), respectively, where l is a characteristic length scale, taken to be the injector diameter and I the turbulence intensity taken as 5% from a sensitivity analysis.

$$k_0 = \frac{3}{2}\left(Iu^2\right) \tag{29}$$

$$\epsilon_0 = \frac{c_\mu^{3/4}\kappa^{3/2}}{0.014l} \tag{30}$$

A type–E thermocouple set on a traverse is used to monitor radial temperature profiles. Because the thermocouple's dimensions are of the same order of magnitude as the injector – its bead has a diameter of 1.10 mm, and it is positioned 0.14 mm from the injector's exit plane – flow blockage is expected, which affects the measurements and the expected re-circulation regions, due to the large outer-to-inner jet velocity and momentum ratios.

Table 1 represents the experimental test conditions [11] replicated in the present study. Quasi-isobaric conditions have a pressure ranging from 3.52 to 4.97 MPa, considering inner jet temperature below and above the critical point. In contrast, chamber and outer jet temperatures remain above nitrogen's critical point. Higher outer jet injection velocities lead to fast atomization of the inner jet nitrogen at varying velocity and momentum ratios.

4. Validation

Grid independence studies are depicted in Figs. 2 and 4 for cases 16 and 21, respectively. The radial temperature profiles obtained with the three meshes considered – 3.88×10^5, 7.5×10^5 and 1.5×10^6 points – are depicted in the figures, being the ratio of the radial distance, r

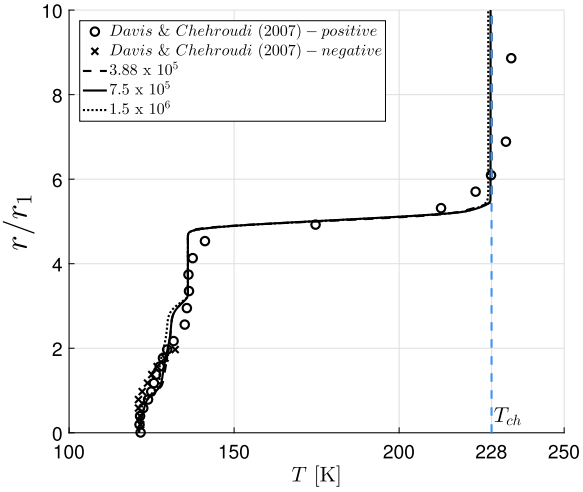

Fig. 2. Grid Independence Study, corresponding to case 16.

to the inner stream radius, r_1 given as a function of the temperature T. The chamber temperature of each experimental configuration [11] is also highlighted, T_{ch}. Two sets of experimental measurements [11] are depicted as positive and negative, corresponding to temperature profiles measured radially [44] from the jet centerline.

Computational error is analyzed through Richardson's extrapolation [45] as the grid is progressively refined in Figs. 3 and 5. The figures depict the numerical error as a function of the grid convergence index [45], showcasing a slope intermediate between the first and second order.

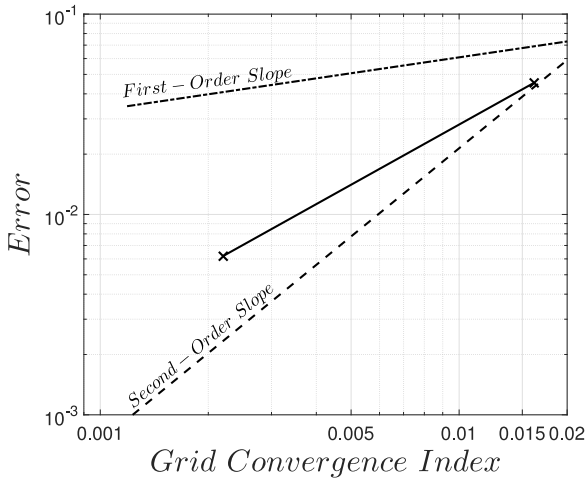

Fig. 3. Error propagation, corresponding to case 16.

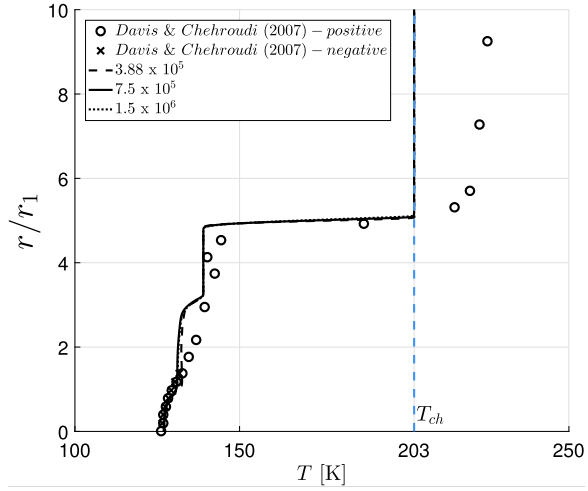

Fig. 4. Grid Independence Study, corresponding to case 21.

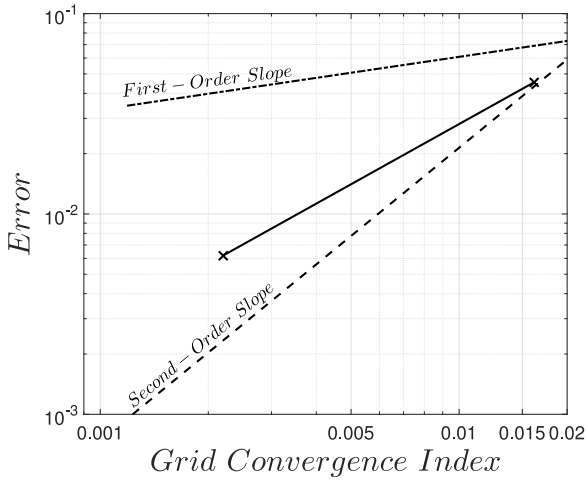

Fig. 5. Error propagation, corresponding to case 21.

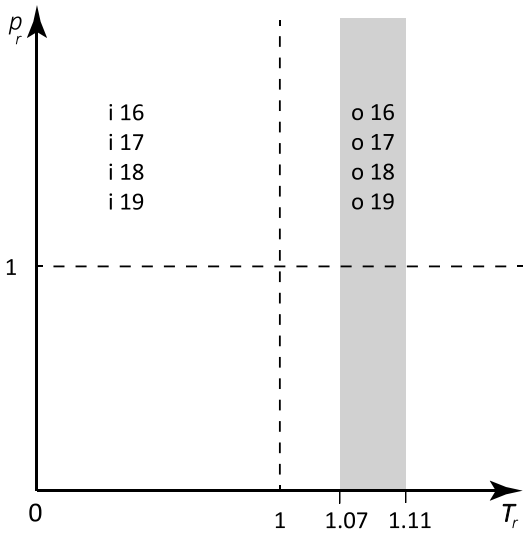

Fig. 6. Supercritical high-temperature case distribution.

5. Results

Fig. 6 depicts the inner and outer jet conditions of cases 16, 17, 18, and 19 concerning the critical point, where p_r and T_r represent reduced pressure and temperature, respectively. The inner jet, denoted by i, is injected under transcritical conditions, meaning a two-phase flow exists. In contrast, the outer jet, denoted by o, is injected under supercritical conditions close to the critical point, as indicated by the reduced temperature range of 1.07 to 1.11.

Figs. 7, 8, 9 and 10 detail the radial temperature profiles for cases 16, 17, 18 and 19 of Table 1. The radial distance measured from the jet, r axis is divided by the main stream radius r_1. It is possible to observe in the figures that due to the thermal stratification taking place in the injector at supercritical liquid- and gas-like conditions [7,20], the temperature starts to vary at $r/r_1 = 0$, in accordance to the experimental data [11], both in the positive and negative directions. Furthermore, it contrasts with the LES results of [23] for case 16 in Fig. 7, where a potential core is depicted. This is explained due to neglecting the heat transfer inside the injector, with the imposition of plug flow profiles of velocity and temperature following a purely mechanical description of supercritical jet breakup [7]. Moreover, given the range of momentum and velocity ratios considered (Table 1), leading to the entrainment of high speed nitrogen from the coaxial stream into the lower speed stream, two counter-rotating vortices are formed in the post tip between both streams, corresponding to the region $2 < r/r_1 < 4$ in Figs. 7 to 10 where there is some discrepancy between the experimental data the present numerical computations. This is attributed to the thermocouple's bead [11], whose diameter (0.1 mm) is of the same order of magnitude as the injector diameter (0.508 mm for the inner stream inner diameter), which perturbs the flow and the re-circulations formation.

Another set of experimental conditions from Table 1 is summarized in Fig. 11, increasing chamber pressure to around 5 MPa and the inner jet injection temperature above nitrogen's critical point values. The obtained radial temperature profiles of the two test cases (20 and 21) are depicted in Figs. 12 and 13.

From Fig. 12, it is possible to observe an experimental temperature at the jet axis lower than the inner jet injection temperature (128 K in Table 1). Given that out of all the cases in the experimental dataset, this was attributed to some typo and a new computation was performed with the injection temperature depicted by the experimental

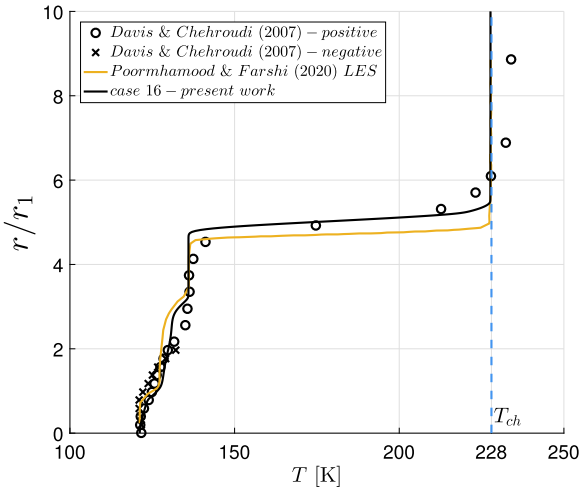

Fig. 7. Case 16 temperature profile (radial).

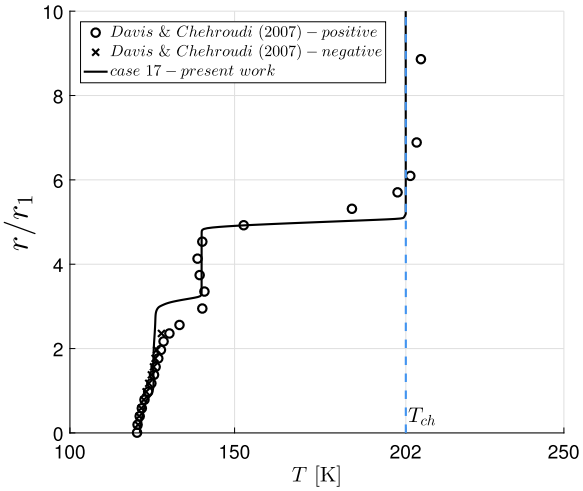

Fig. 8. Case 17 temperature profile (radial).

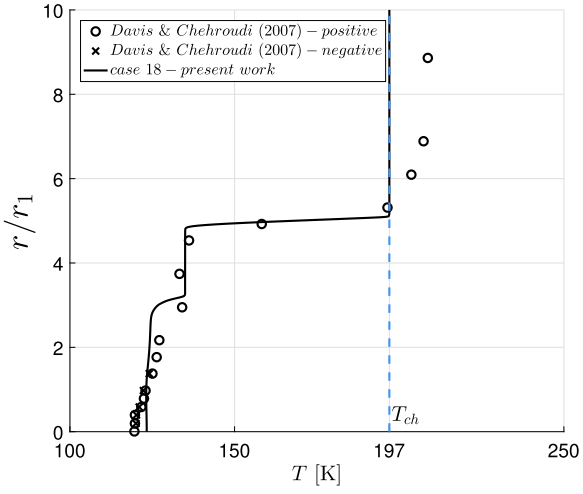

Fig. 9. Case 18 temperature profile (radial).

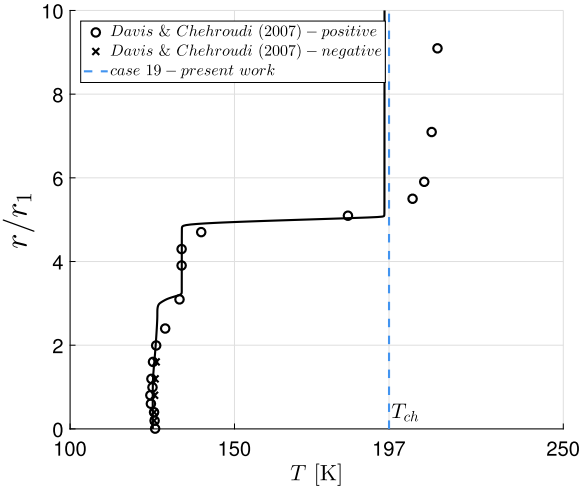

Fig. 10. Case 19 temperature profile (radial).

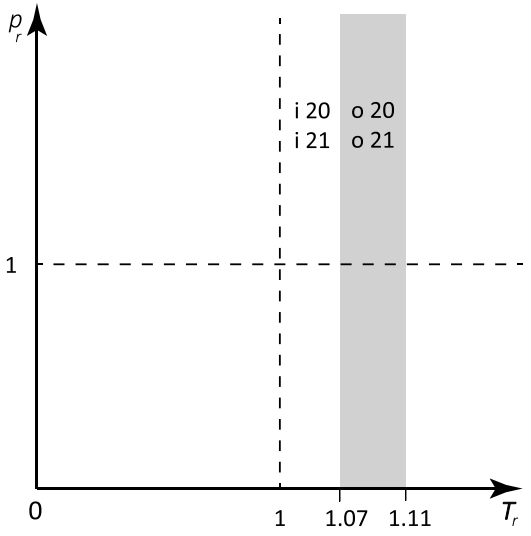

Fig. 11. Supercritical high-temperature case distribution.

profile at the jet axis (119 K, lower than nitrogen's critical temperature at 126.8 K). As depicted in the figure, the fitted temperature constitutes a closer approximation to the experimental profile. The higher momentum ratio effect is seen in Figs. 12 and 13 While in case 20, the outer-to-inner jet momentum ratio is of 0.8, smaller counter-rotating re-circulation regions are anchored to the injector post tip between $2 < r/r_1 < 4$, leading to a smaller degree of intrusion by the thermocouple to the flow, in case 21 the momentum ratio increases to 6.3, augmenting the size of the re-circulation region, where the thermocouple's intrusive behavior will be more relevant as indicated by the numerical temperature profile in Fig. 13.

The last set of experimental test cases considered in this study is depicted in Fig. 14 for cases 9, 10, 11, and 12. Here the temperature of the outer jet is increased to a range of reduced values between 1.47 and 1.58, while inner jet injection conditions are of the same order of magnitude as those for cases 20 and 21.

Figs. 15, 16, 17 and 18 depict the results for cases 9, 10, 11 and 12, respectively. As the outer-to-inner jet momentum ratio increases from 0.5 in case 9 to 9.6 in case 12, the size of the re-circulation region increases in the same way as for cases 16–19. However, the temperature range in which the outer jet is injected increased from a

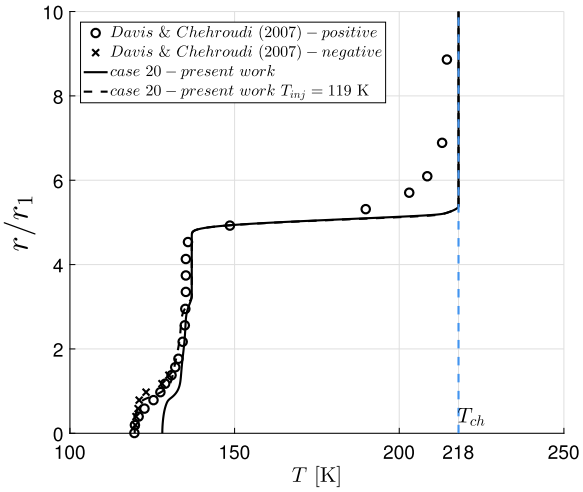

Fig. 12. Case 20 temperature profile (radial).

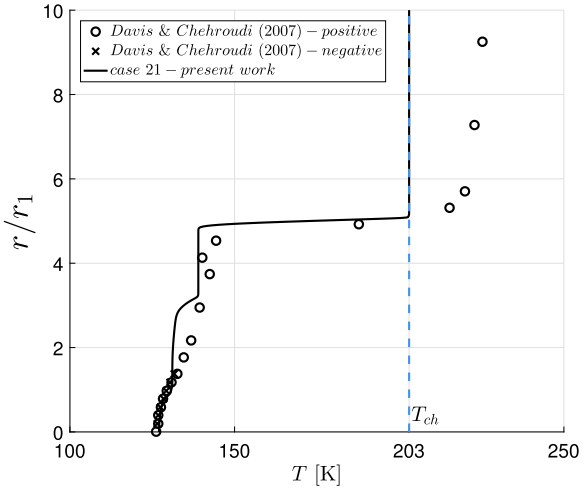

Fig. 13. Case 21 temperature profile (radial).

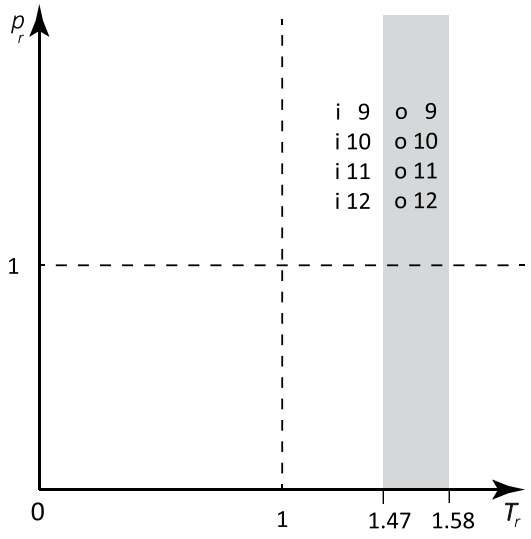

Fig. 14. Supercritical high-temperature case distribution.

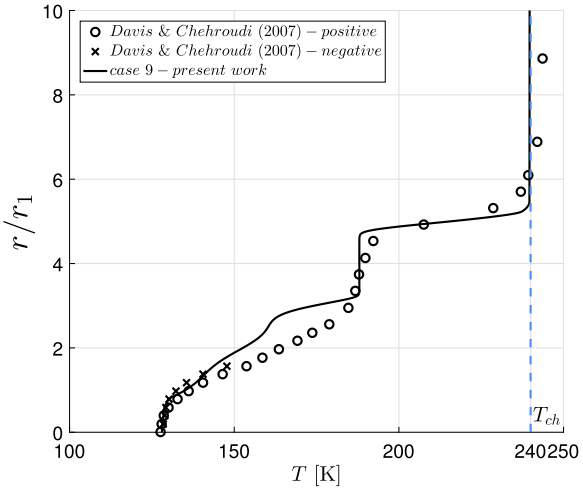

Fig. 15. Case 9 temperature profile (radial).

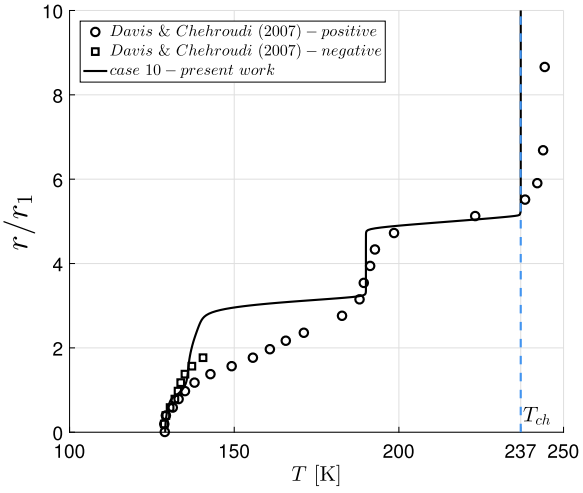

Fig. 16. Case 10 temperature profile (radial).

reduced temperature range between 1.07 and 1.11 in the previously described test cases to a range between 1.47 to 1.58 in cases 9 through 12. At these gas-like supercritical conditions, the energy received by the jet does not mainly contribute to its expansion since the thermal shield [8] in the form of the peak in the isobaric specific heat does not need to be overcome by increasing mixing efficiency, where thermal effects assume a more preponderant role than momentum transfer.

The re-circulation region anchoring to the injector post tip is highlighted in Figs. 19 and 20 for cases 10 and 11, respectively. Fig. 19 depicts the velocity field for case 10, with an outer-to-inner jet velocity ratio of 3.6 and momentum ratio of 2.7, following Table 1, where it is possible to observe the presence of two counter-rotating re-circulations at the injector post tip and Fig. 20 details the velocity field of case 11, for a momentum ratio of 5.1 and a velocity ratio of 4.3. The figures show that the increase in velocity ratio contributed to a change in the re-circulation axial positioning from 2.5 to 3 inner injector diameters. In general, when the outer stream velocity rises, mixing improves, lowering potential core length and enhancing jet spreading, which is more obvious for temperature than for density [20], suggesting that heat propagation is more important than momentum transmission.

Fig. 21 depicts a comparison between a fitted case 12, where the velocity of the inner jet was increased to $32\,\mathrm{m\,s^{-1}}$ and the outer one

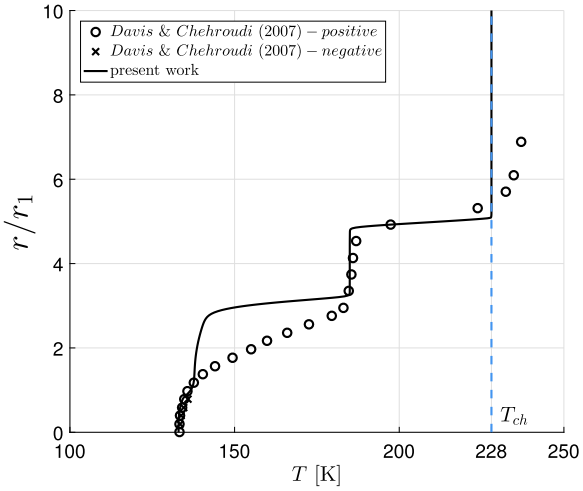

Fig. 17. Case 11 temperature profile (radial).

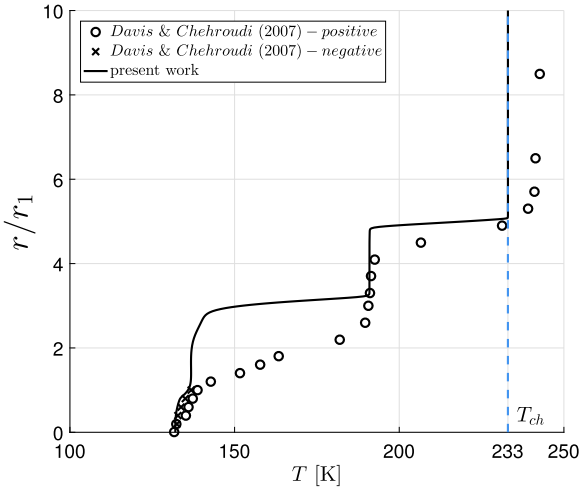

Fig. 18. Case 12 temperature profile (radial).

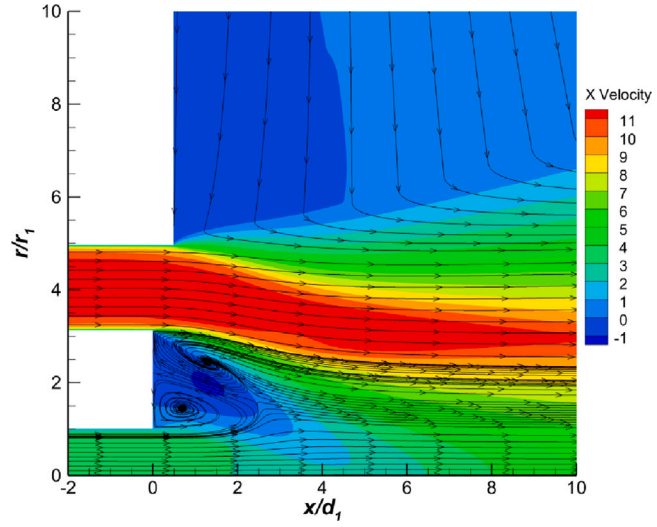

Fig. 19. Case 10 velocity field and re-circulation.

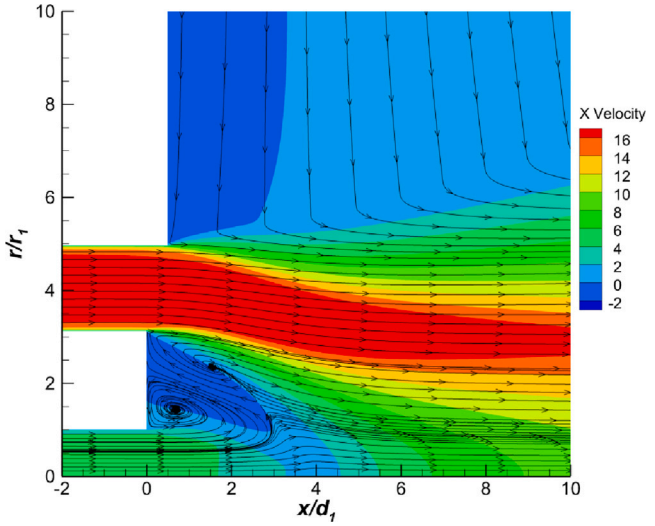

Fig. 20. Case 11 velocity field and re-circulation.

to 120 m s^{-1}, to match the space shuttle main engine (SSME) pre burner, following previous LES studies in the literature [46]. Since the outer and inner jet injection velocities were increased tenfold, the axial distance in which the radial temperature profile was extracted was also increased by the same scale [46]. This allows us to perform some sort of comparison in a region of the jet further downstream without the influence of the re-circulation region and the thermocouple's disturbance. In the figure, the experimental temperature profiles for cases 9 through 12 are also included for comparison, and it is possible to observe a very similar radial profile between the present computations and the LES technique.

6. Conclusions

Nitrogen under supercritical conditions is modeled following a coaxial configuration at varying outer-to-inner velocity and momentum ratios characteristic of those encountered in the typical operation of liquid-propelled rocket engines. Two counter-rotating re-circulation regions are formed at the injector post tip, characterized by the formation of two shear layers. As the momentum ratio increases, mixing is enhanced, increasing jet spreading, which is more pronounced in terms of temperature than for momentum, further validating previous works.

A comparison with canonical experiments highlights a good agreement with the present computations. A vigorous mixing in the shear layer is reported due to the high outer-to-inner jet momentum ratios considered. Moreover, the similar dimensions of the injector diameter and the thermocouple's head are responsible for a degree of departure between experimental and numerical data in the re-circulation region.

The consideration of injector flow in the computations proved to be paramount to retrieve more realistic inflow conditions at the chamber's inlet in terms of velocity and temperature, which led to radial temperature profiles exhibiting a temperature increase starting from the jet axis, conversely to what was previously reported in the literature for density.

Lastly, further comparisons with more sophisticated techniques, such as LES, showed good agreement for the nitrogen jet radial temperature profiles, highlighting the current approach's suitability for evaluating mean quantities. In the future, multi-species mixing will be considered, and fundamental research at the DNS level will be carried out to broaden the knowledge regarding supercritical injection phenomena.

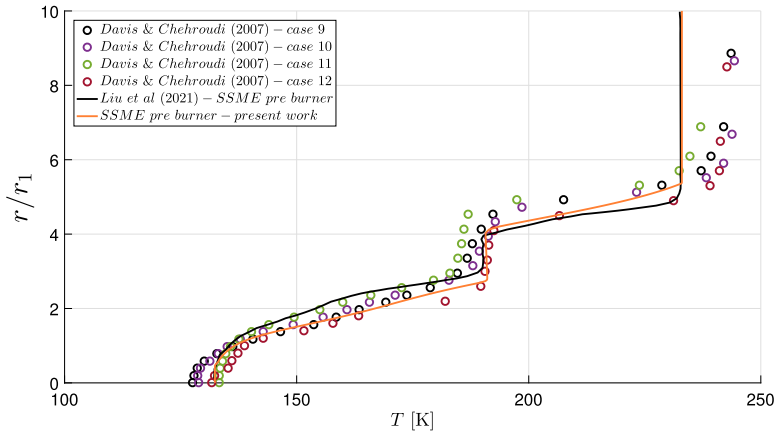

Fig. 21. SSME pre-burner simulation and comparison with LES results [46].

Declaration of competing interest

The authors declare that they have no known competing financial interests or personal relationships that could have appeared to influence the work reported in this paper.

Acknowledgments

The present work was performed under the scope of activities at the Aeronautics and Astronautics Research Center (AEROG) of the Laboratório Associado em Energia, Transportes e Aeronáutica (LAETA), and was supported by the Fundação para a Ciência e Tecnologia (Grant No. SFRH/BD/136381/ 2018, Project No. UIDB/50022/2020).

References

[1] C. Traxinger, J. Zips, M. Pfitzner, Single-phase instability in non-premixed flames under liquid rocket engine relevant conditions, J. Propuls. Power 35 (4) (2019) 1–15, http://dx.doi.org/10.2514/1.B37395.

[2] S. Jiao, S. Li, H. Pu, M. Dong, Y. Shang, Investigation of pyrolysis effect on convective heat transfer characteristics of supercritical aviation kerosene, Acta Astronaut. 171 (2020) 55–68, http://dx.doi.org/10.1016/j.actaastro.2020.02.049.

[3] M. Sahami, H. Ghassemi, Effects of non-equilibrium condensation on the nozzle performance of a cold gas thruster, Acta Astronaut. 197 (2022) 200–216, http://dx.doi.org/10.1016/j.actaastro.2022.05.032.

[4] V. Yang, Modeling of supercritical vaporization, mixing, and combustion processes in liquid-fueled propulsion systems, Proc. Combust. Inst. 28 (1) (2000) 925–942, http://dx.doi.org/10.1016/S0082-0784(00)80299-4.

[5] B. Chehroudi, Recent experimental efforts on high-pressure supercritical injection for liquid rockets and their implications, Int. J. Aerosp. Eng. 2012 (2012) 1–31, http://dx.doi.org/10.1155/2012/121802.

[6] D.T. Banuti, Crossing the widom-line – Supercritical pseudo-boiling, J. Supercritical Fluids 98 (2015) 12–16, http://dx.doi.org/10.1016/j.supflu.2014.12.019.

[7] D.T. Banuti, K. Hannemann, The absence of a dense potential core in supercritical injection: A thermal break-up mechanism, Phys. Fluids 28 (3) (2016) 035103, http://dx.doi.org/10.1063/1.4943038.

[8] C. Lagarza-Cortés, J. Ramírez-Cruz, M. Salinas-Vázquez, W. V.-Rodríguez, J.M. Cubos-Ramírez, Large-eddy simulation of transcritical and supercritical jets immersed in a quiescent environment, Phys. Fluids 31 (2) (2019) 025104, http://dx.doi.org/10.1063/1.5054797.

[9] W. Mayer, J. Telaar, R. Branam, G. Schneider, J. Hussong, Raman measurements of cryogenic injection at supercritical pressure, Heat Mass Transf. 39 (8–9) (2003) 709–719, http://dx.doi.org/10.1007/s00231-002-0315-x.

[10] M. Oschwald, A. Schik, Supercritical nitrogen free jet investigated by spontaneous Raman scattering, Exp. Fluids 27 (6) (1999) 497–506, http://dx.doi.org/10.2514/6.1999-2887.

[11] D.W. Davis, B. Chehroudi, Measurements in an acoustically driven coaxial jet under sub-, near-, and supercritical conditions, J. Propuls. Power 23 (2) (2007) 364–374, http://dx.doi.org/10.2514/1.19340.

[12] H. Müller, C.A. Niedermeier, J. Matheis, M. Pfitzner, S. Hickel, Large-eddy simulation of nitrogen injection at trans- and supercritical conditions, Phys. Fluids 28 (1) (2016) 015102, http://dx.doi.org/10.1063/1.4937948.

[13] F. Ries, P. Obando, I. Shevchuck, J. Janicka, A. Sadiki, Numerical analysis of turbulent flow dynamics and heat transport in a round jet at supercritical conditions, Int. J. Heat Fluid Flow 66 (2017) 172–184, http://dx.doi.org/10.1016/j.ijheatfluidflow.2017.06.007.

[14] P.E. Lapenna, Characterization of pseudo-boiling in a transcritical nitrogen jet, Phys. Fluids 30 (7) (2018) 77–106, http://dx.doi.org/10.1063/1.5038674.

[15] P.E. Lapenna, F. Creta, Direct numerical simulation of transcritical jets at moderate Reynolds number, AIAA J. 57 (6) (2019) 2254–2263, http://dx.doi.org/10.2514/1.J058360.

[16] N. Kim, Y. Kim, Large eddy simulation based multi-environment PDF modelling for mixing processes of transcritical and supercritical cryogenic nitrogen jets, Cryogenics 110 (2020) 103134, http://dx.doi.org/10.1016/j.cryogenics.2020.103134.

[17] J. Ma, H. Liu, L. Liu, M. Xie, Simulation study on the cryogenic liquid nitrogen jets: Effects of equations of state and turbulence models, Cryogenics 117 (2021) 103330, http://dx.doi.org/10.1016/j.cryogenics.2021.103330.

[18] J.V.M. Gopal, G. Tretola, R. Morgan, G. de Sercey, G. Lamanna, K. Vogiatzaki, Unpicking the interplay of turbulence, diffusion, and thermophysics in cryogenic jets at supercritical pressures, Phys. Fluids 33 (7) (2021) 077106, http://dx.doi.org/10.1063/5.0056509.

[19] F. Ries, A. Sadiki, Supercritical and transcritical turbulent injection processes: Consistency of numerical modeling, Atomization Sprays 31 (5) (2021) 37–71, http://dx.doi.org/10.1615/AtomizSpr.2021035399.

[20] L.B. Magalhães, A.R.R. Silva, J.M.M. Barata, Contribution to the physical description of supercritical cold flow injection: The case of nitrogen, Acta Astronaut. (190) (2022) 251–260.

[21] A. Hosangadi, C.P. Lee, C. Kannepalli, S. Arunajatesan, Three-dimensional hybrid RANS/LES simulations of a supercritical liquid nitrogen jet, in: 44th AIAA/ASME/SAE/ASEE Joint Propulsion Conference & Exhibit, 2008, http://dx.doi.org/10.2514/6.2008-5227.

[22] T. Schmitt, J. Rodriguez, I.A. Leyva, S. Candel, Experiments and numerical simulation of mixing under supercritical conditions, Phys. Fluids 24 (5) (2012) 55–104, http://dx.doi.org/10.1063/1.3701374.

[23] A. Poormahmood, M. Farshchi, Numerical study of the mixing dynamics of trans- and supercritical coaxial jets, Phys. Fluids 32 (12) (2020) 125105, http://dx.doi.org/10.1063/5.0030183.

[24] M. Liu, J. Tang, S. Liu, D. Xi, L. Min, J. Zang, G. Liu, J. Wang, S. Huang, Y. Huang, Modified Landau model for fluids: A rethink of pseudoboiling theory for supercritical fluids, J. Supercrit. Fluids 183 (2022) 105554, http://dx.doi.org/10.1016/j.supflu.2022.105554.

[25] G. Buresti, A. Talamelli, P. Petagna, Experimental characterization of the velocity field of a coaxial jet configuration, Exp. Therm Fluid Sci. 9 (2) (1994) 135–146, http://dx.doi.org/10.1016/0894-1777(94)90106-6.

[26] E. Villermaux, Mixing and spray formation in coaxial jets, J. Propuls. Power 14 (5) (1998) 807–817, http://dx.doi.org/10.2514/2.5344.

[27] H. Rehab, E. Villermaux, E. Hopfinger, Flow regimes of large-velocity-ratio coaxial jets, J. Fluid Mech. (345) (1997) 357–381.

[28] V. Betelin, A. Kushnirenko, N. Smirnov, V. Nikitin, V. Tyurenkova, L. Stamov, Numerical investigations of hybrid rocket engines, Acta Astronaut. 144 (2018) 363–370, http://dx.doi.org/10.1016/j.actaastro.2018.01.009.

[29] V.V. Tyurenkova, L.I. Stamov, Flame propagation in weightlessness above the burning surface of material, Acta Astronaut. 159 (2019) 342–348, http://dx.doi.org/10.1016/j.actaastro.2019.03.053.

[30] A. Kushnirenko, L. Stamov, V. Tyurenkova, M. Smirnova, E. Mikhalchenko, Three-dimensional numerical modeling of a rocket engine with solid fuel, Acta Astronaut. 181 (2021) 544–551, http://dx.doi.org/10.1016/j.actaastro.2021.01.028.

[31] M. Oschwald, A. Schik, M. Klar, W. Mayer, Investigation of coaxial LN2/GH2-injection at supercritical pressure by spontaneous Raman scattering, in: 35th Joint Propulsion Conference and Exhibit, 1999, http://dx.doi.org/10.2514/6.1999-2887.

[32] B.E. Launder, D.B. Spalding, Lectures in Mathematical Models of Turbulence, Academic Press, London, England, 1972.

[33] D. Peng, D.B. Robinson, A new two-constant equation of state, Ind. Eng. Chem. Fundam. 15 (1) (1976) 59–64, http://dx.doi.org/10.1021/i160057a011.

[34] J.C. Oefelein, Thermophysical characteristics of shear-coaxial LOX–H2 flames at supercritical pressure, Proc. Combust. Inst. 30 (2) (2005) 2929–2937, http://dx.doi.org/10.1016/j.proci.2004.08.212.

[35] R.C. Reid, J.M. Prausnitz, B.E. Poling, the Properties of Gases and Liquids, McGraw-Hill, Inc, 1987.

[36] B.J. McBride, M.J. Zehe, S. Gordon, NASA Glenn Coefficients for Calculating Thermodynamic Properties of Individual Species, Technical Report NASA/TP–2002-211556, NASA Glenn Research Center, 2002.

[37] E.W. Lemmon, R.T. Jacobsen, Viscosity and thermal conductivity equations for nitrogen, oxygen, argon and air, Int. J. Thermophys. 25 (1) (2004) 21–69, http://dx.doi.org/10.1023/B:IJOT.0000022327.04529.f3.

[38] G.A. Olchowy, J.V. Sengers, A simplified representation for the thermal conductivity of fluids in the critical region, Int. J. Thermophys. 10 (2) (1989) 417–426, http://dx.doi.org/10.1007/BF01133538.

[39] B.P. Leonard, A stable and accurate convective modelling procedure based on quadratic upstream interpolation, Comput. Methods Appl. Mech. Engrg. (1979) 58–98, http://dx.doi.org/10.1016/0045-7825(79)90034-3.

[40] G. Lacaze, T. Schmitt, A. Ruiz, J.C. Oefelein, Comparison of energy-, pressure- and enthalpy-based approaches for modeling supercritical flows, Comput. & Fluids 181 (2019) 35–56, http://dx.doi.org/10.1016/j.compfluid.2019.01.002.

[41] J. Hickey, P.C. Ma, M. Ihme, S. Thakur, Large eddy simulation of a shear coaxial rocket injector: Real fluid effects, in: 49th AIAA/ASME/SAE/ASEE: Joint Propulsion Conference, 2013, http://dx.doi.org/10.2514/6.2013-4071.

[42] M. Jarczyk, M. Pfitzner, Large eddy simulation of supercritical nitrogen jets, in: 50th AIAA Aerospace Sciences Meeting, 2012, http://dx.doi.org/10.2514/6.2012-1270.

[43] D. Kendrick, G. Herding, P. Scouflaire, C. Rolon, S. Candel, Effects of a Recess on cryogenic flame stabilization, Combust. Flame 118 (3) (1999) 327–339, http://dx.doi.org/10.1016/S0010-2180(98)00168-0.

[44] D. Davis, On the Behavior of a Shear-coaxial Jet, Spanning Sub- to Supercritical Pressures, with and without an Externally Imposed Transverse Acoustic Field (Ph.D. thesis), The Pennsylvania State University, 2006.

[45] P.J. Roache, Verification and Validation in Computational Science and Engineering, John Whiley & Sons, Albuquerque, New Mexico, 1998.

[46] T. Liu, X. Wang, V. Yang, Flow dynamics of shear-coaxial cryogenic nitrogen jets under supercritical conditions with and without acoustic excitations, Phys. Fluids 33 (7) (2021) 076111, http://dx.doi.org/10.1063/5.0054435.